IEEE Open Journal of Vehicular Technology

Received 7 November 2023; accepted 30 November 2023. Date of publication 6 December 2023;
date of current version 22 December 2023. The review of this article was coordinated by Editor Koichi Adachi.

Digital Object Identifier 10.1109/OJVT.2023.3339799

An Empirical Study on Channel Reciprocity in TDD and FDD Systems

HUIXIN XU [1] (Graduate Student Member, IEEE), JIANHUA ZHANG [1] (Senior Member, IEEE), PAN TANG [1] (Member, IEEE), LEI TIAN [1] (Member, IEEE), QIXING WANG [2], AND GUANGYI LIU [2] (Member, IEEE)

[1]State Key Lab of Networking and Switching Technology, Beijing University of Posts and Telecommunications, Beijing 100876, China
[2]China Mobile Research Institute, Beijing 100053, China

CORRESPONDING AUTHORS: JIANHUA ZHANG; PAN TANG (e-mail: jhzhang@bupt.edu.cn; tangpan27@bupt.edu.cn).

This work was supported in part by the National Science Foundation for Distinguished Young Scholars under Grant 61925102, in part by the National Natural Science Foundation of China under Grants 92167202, 62201086, 62101069, and 62201087, and in part by the Beijing University of Posts and Telecommunications-China Mobile Research Institute Joint Innovation Center.

ABSTRACT The 6 GHz band plays a crucial role in the development of the 6G. A profound comprehension of channel reciprocity is essential for designing time division duplexing/frequency division duplexing (TDD/FDD) systems within this band. Firstly, in an indoor corridor scenario, precise and impartial measurements are conducted for both the uplink (UL) and downlink (DL) channels in the 6 GHz band; A denoising algorithm is proposed to extract multipath components (MPCs) from the measurement data, enabling a more equitable assessment of channel reciprocity; Then, a comprehensive analysis of channel reciprocity has been conducted, focusing on four aspects: path loss, delay spread, cluster-based correlation coefficient (CBCC), and multipath power dissimilarity (MPD). The findings indicate that TDD systems demonstrate nearly perfect reciprocity, whereas FDD systems exhibit partial reciprocity in indoor scenarios. Specifically, in TDD systems, the CBCCs between UL and DL exceed 95%, while in FDD systems, they fluctuate between 80% and 90%. Additionally, a model has been provided to depict the relationship between MPD and center frequency, as well as frequency interval; Finally, a comparative analysis of measured and ray-tracing simulated results reveals the presence of numerous public MPCs, which share the same propagation delay and spatial angle between the UL and DL in FDD systems, as well as private MPCs that exist exclusively in either the UL or DL. They collectively influence the channel reciprocity.

INDEX TERMS 6G, 6 GHz band, channel measurement, channel reciprocity, frequency division duplexing (FDD), time division duplexing (TDD).

I. INTRODUCTION

The success of the 6G will hinge on the integrated exploitation of spectrum across various frequency ranges, encompassing sub-6 GHz, new mid-band, millimeter-wave (mmWave), and terahertz bands. In order to strike a balance between capacity and coverage, it is imperative to fully leverage the new mid-band within the 6–15 GHz frequency range [1]. Notably, the 6 GHz band, spanning from 5925 to 7125 MHz, constitutes a pivotal component of the new mid-band spectrum [2]. The International Telecommunication Union (ITU) is set to deliberate on the potential identification of International Mobile Telecommunications (IMT) within the frequency band of 6.425–7.125 GHz at the World Radiocommunication Conference in 2023 [3]. This pivotal step signifies a monumental achievement in the establishment of IMT allocation for the 6 GHz band, paving the way for it to be considered a prospective frequency band for 6G networks.

Previous generations of mobile communication systems have predominantly utilized two duplex technologies: time division duplexing (TDD) and frequency division duplexing (FDD) [4]. In FDD systems, a pair of bands is designated for both downlink (DL) – where the base station (BS) transmits and the user equipment (UE) receives signals – and uplink (UL), where the UE transmits and the BS receives signals. In contrast, TDD systems do not require a pair of bands. They

utilize different time slots within the same frequency band to differentiate between the DL and UL.

Channel reciprocity refers to the property in wireless communication where the characteristics of the UL and DL channels between two nodes are symmetric or equivalent [5]. This means that the fading and propagation properties experienced by transmitted signals are the same in both directions. The reciprocity between UL and DL channels stands as a primary determinant influencing the distinct developmental trajectories of these two duplex technologies. Many studies perform channel estimation based on the reciprocity of the channel [6], [7]. When the UL and DL channels exhibit reciprocity, the channel state information (CSI) of the DL can be obtained through channel estimation based on UL pilots. When reciprocity is lacking between the UL and DL channels, it introduces challenges in implementing the acquisition process for DL CSI. This non-reciprocity stems from two primary factors [8]. First, UL and DL operate on different frequency bands, and the varying propagation characteristics of electromagnetic waves contribute to a non-reciprocal propagation channel. Additionally, The asymmetrical characteristics of the radio frequency transmission and receiving chains also contribute to the non-reciprocity of radio channels [9].

It is conventionally held that TDD systems exhibit reciprocity, while FDD systems do not [10]. In addressing the challenge of non-reciprocal channel estimation, numerous scholars have contemplated whether it is feasible to directly infer the DL CSI from the observed information on the UL channel [6], [11]. One key approach is to extrapolate the physical parameters from the UL channel, identifying frequency-related parameters. This enables the reconstruction of the DL channel based on the information obtained from the UL channel [7], [12]. Consequently, it is of considerable importance to investigate the reciprocity of TDD/FDD systems in the 6 GHz band.

Various studies have analyzed the reciprocity of TDD/FDD systems through extensive channel measurements. In TDD systems, factors such as human movement, vehicular traffic [13], transceiver environments, and antenna height [14] can disrupt channel reciprocity. Furthermore, the analysis of the channel matrix obtained from measurements of the TDD prototype system indicates that as the channel from line-of-sight (LoS) to partial obstruction by foliage, and further to full-blocked non-line-of-sight (NLoS), the channel correlation gradually diminishes [15]. Regarding FDD systems, channel measurements demonstrate that the azimuth angle of arrival for the main propagation paths at 1935 and 2125 MHz in the UL and DL bands respectively are approximately the same. This substantiates the existence of spatial reciprocity between the adjacent bands [16]. In a study [17], it is deduced that all multipath parameters–angle, delay, and complex fading factor (amplitude)–between UL and DL channels remain frequency-independent, affirming their reciprocity. Nevertheless, theoretical analysis has established that not all multipath parameters for DL and UL channels are identical. This theoretical insight has been substantiated through a channel measurement campaign, demonstrating the presence of partial reciprocity [18].

The existing literature attempt to address the question of whether the UL and DL channels in TDD/FDD systems exhibit reciprocity. However, there is no consensus on whether TDD/FDD systems are reciprocal. This stems from several factors: first, the accuracy and impartiality of the channel measurement campaigns are lacking. These measurements do not sufficiently eliminate the influences of radio frequency links and transceiver antennas [15], and fail to ensure the static nature of the measurement scenarios [14]; Second, an inequitable post-processing of channel measurement raw data introduces bias in reciprocity analysis. For instance, the extraction and denoising of channel impulse response (CIR) [19]; Additionally, assessing reciprocity solely from a single aspect or metric makes it challenging to accurately determine channel reciprocity [20]; Finally, there has not been a sufficiently in-depth exploration of the factors influencing reciprocity from the perspective of physical propagation of radio waves, particularly in terms of multipath components (MPCs). Most of the existing studies focus on channel statistical characteristics, encompassing path loss, shadow fading, root mean square (RMS) delay spread, angle spread, and others [14], [16], [18]. However, the power delay profile (PDP) and power angular delay profile (PADP), which carry information about parameters such as multipath power, delay, and angles, have not been thoroughly investigated. These parameters are better aligned with the application demands of channel reciprocity in channel estimation.

Therefore, we design and conduct precise and impartial channel measurements in the 6 GHz band within indoor corridor scenarios. Subsequently, a denoising algorithm is proposed to extract MPCs from the CIR. Then, based on the processed data, a comprehensive analysis of the reciprocity is performed from four aspects: path loss, delay spread, correlation coefficient, and multipath power differences. Finally, factors influencing reciprocity are then expounded upon in terms of multipath propagation. The primary contributions of this article can be summarized as follows:

- A precise and impartial channel measurement campaign for both UL and DL has been designed and implemented in the 6 GHz band. It provides a reliable channel measurement database crucial for the reciprocity analysis of TDD/FDD systems. Additionally, a CIR denoising algorithm has been proposed, further enhancing the groundwork for a more equitable exploration of channel reciprocity.
- A comprehensive analysis of reciprocity between the UL and DL channels in TDD/FDD systems is conducted, considering four aspects: path loss, delay spread, correlation coefficient, and multipath power dissimilarity (MPD). The findings indicate that TDD systems demonstrate near-perfect reciprocity, while FDD systems display partial reciprocity. Furthermore, a model has been developed to depict the MPD's dependence on center frequency and frequency interval.

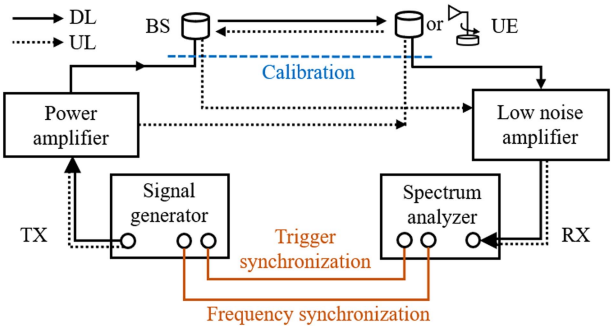

FIGURE 1. Diagram of UL and DL channel sounder.

- Ray-tracing simulations with the same configurations as the measurements are conducted to provide multipath parameters and propagation trajectories for the analysis of reciprocity's influencing factors. It can be inferred that in FDD systems, there are numerous public MPCs in both the UL and DL channels, sharing the same propagation delay and angle, as well as private MPCs that exist exclusively in either the UL or DL. These collectively influence channel reciprocity.

The subsequent sections of this article are organized as follows: Section II provides an overview of channel measurement and data processing. In Section III, a denoising algorithm for CIR is proposed. Section IV delves into a comprehensive analysis of channel reciprocity. Section V analyzes the factors influencing channel reciprocity, focusing on multipath delay and angle. Finally, the conclusion of this article is drawn in Section VI.

II. CHANNEL MEASUREMENTS AND DATA PROCESSING

Channel measurements serve as a direct and efficient approach for acquiring channel characteristics [21], [22]. This section outlines a channel reciprocity measurement campaign conducted in the 6 GHz band in indoor corridor scenarios, along with the associated data processing procedures. The UL and DL channels are acquired through the reciprocal swapping of roles between the transmitter (TX) and receiver (RX).

A. CHANNEL MEASUREMENTS

During the channel measurements, a wideband correlation-based time-domain channel sounder is utilized, with the structure of the measurement system depicted in Fig. 1. The pseudo-random (PN) sequence is adopted as the sounding signal for its superior approximation to the Dirac delta function in autocorrelation, in addition to its straightforward generation process and wide dynamic range [1], [23]. On the TX side, the signal generator sequentially generates a PN sequence at four center frequency bands (6, 6.5, 7, and 7.5 GHz). On the RX side, the spectrum analyzer captures and records signals from these four frequency bands for subsequent analysis. Due to the separation of the time-domain channel sounder between the TX and RX, it is imperative to establish connections for trigger synchronization and frequency synchronization, thereby ensuring the precision and consistency of UL and DL channel measurements. In order to expand signal coverage and enhance the signal-to-noise ratio (SNR), a power amplifier and low-noise amplifier are integrated into the TX and RX, respectively [24]. Additionally, calibration is necessary after the sounder is assembled to remove the system response.

TABLE 1. Measurement Configuration

Parameter	Value
Center frequency	6 GHz 6.5 GHz 7 GHz 7.5 GHz
Bandwidth	200 MHz
PN sequence length	511
Sampling rate	200 MSa/s
Delay resolution	5 ns
BS/UE antenna type	Discone / Discone (Horn)
BS/UE antenna height	1.95 m / 1.3 m
Horn antenna azimuth HPBW	30°
Horn antenna rotation step	5°

Unlike traditional channel characteristics studies that only require measuring the DL channel, this article necessitates measurements of both the UL and DL to investigate their reciprocity. Consequently, both the BS and the UE assume the roles of TX and RX. However, the channel sounder is only capable of single-link (either UL or DL) measurements and cannot support double-link (both UL and DL) channel measurements where BS/UE simultaneously transmit and receive signals. Consequently, measurements of the UL and DL channels are conducted separately. After completing the UL measurements (i.e., the UE connected to the channel sounder's TX, and the BS connected to its RX), DL measurements are then conducted (i.e., BS connected to the TX and UE connected to the RX). It is important to note that the antennas of the BS and UE remain unchanged during this process. The switching of TX and RX is conducted without powering down to ensure consistent performance of the channel sounder during both UL and DL measurements.

Two measurement cases are designed. In the first case, discone antennas are employed on both the BS and UE to capture omnidirectional MPCs. In the second case, while the BS still uses a discone antenna, the UE utilizes a rotating horn antenna with a half-power beamwidth (HPBW) of 30° to further obtain angular information of MPCs. Details of the experimental setup are listed in Table 1.

The channel measurements are carried out within an indoor corridor situated on the 9th floor of the research building at Beijing University of Posts and Telecommunications. This indoor corridor is selected for its abundance of MPCs, and it presents a more challenging environment for achieving UL and DL channel reciprocity [25]. As depicted in Fig. 2, the corridor features a rectangular structure with a dimension of 52 m (length) by 2.08 m (width) by 2.2 m (height). The sidewalls are constructed from concrete and painted with lime. The ceiling is comprised of plasterboard, and the floor is tiled.

FIGURE 2. Measurement photographs taken in (a) the LoS scenario, and (b) the NLoS scenario.

The floor-to-ceiling windows are positioned at both the front and rear ends of the corridor. Furthermore, along the two sidewalls, there are 15 closed office doors and five pilasters.

The measurement layout is illustrated in Fig. 3. In this figure, the red and blue pentagrams represent the positions of the BS for LoS and NLoS scenarios (with the NLoS BS located deep within the L-shaped corridor), respectively. The circles indicate the positions of the UE. All circles indicate LoS points, while the blue-red circles denote NLoS points in case 1. Additionally, the circle marked with a checkerboard texture serves as a horn antenna rotation point in case 2. There are a total of 13 UE measurement points for the LoS scenario and 7 for the NLoS scenario, with distances between the BS and UE ranging from 4 to 40 m. The distance between two adjacent UE measurement points is 3 m, except for the first and second points. Moreover, it is worth noting that the channel reciprocity measurements require a completely static environment. As a result, the measurement campaigns are carried out in an unoccupied corridor during nighttime.

B. DATA PROCESSING

The wireless channel is commonly characterized through the double-directional CIR, which is typically mathematically modeled as a summation of MPCs [26]

$$h\left(t,\tau,\Omega_T,\Omega_R\right)=\sum_{l=1}^{L}\left|\beta_l(t)\right|e^{-j\varphi_l(t)}\delta\left(\tau-\tau_l(t)\right)\\ \delta\left(\Omega_T-\Omega_{T,l}(t)\right)\delta\left(\Omega_R-\Omega_{R,l}(t)\right), \quad (1)$$

where L is the number of MPCs. The formula includes the complex amplitude (amplitude β and phase φ, the delay τ, the angle of arrival (AoA) Ω_R, and the angle of departure (AoD) Ω_T, all of which depend on the absolute time, t. The directional CIR, $h(t,\tau,\Omega_R)$ or $h(t,\tau,\Omega_T)$, is the angle-integrated double-directional CIR. The omnidirectional CIR, $h(t,\tau)$, is the angle-integrated directional CIR.

In real channel measurements, the CIR can be obtained by dividing the received signal by the calibration signal in the frequency domain, followed by an inverse Fourier transform (detailed in [1], [27], [28]). The multi-sample omnidirectional CIR, $h(t,\tau)$, is obtained when both the BS and UE utilize omnidirectional antennas in this article. The PDP is the squared magnitudes of the omnidirectional CIR, depicting the multipath power distribution over the delay. It can be calculated as

$$\mathrm{PDP}\left(t,\tau\right)=\left\|h\left(t,\tau\right)\right\|^2, \quad (2)$$

where $\|\cdot\|$ denotes the 2-norm operation. To mitigate the impact of channel noise fluctuations on the extraction of MPCs, averaging is applied to multiple samplings of the PDP. The averaged power delay profile (APDP) can be expressed as

$$\mathrm{APDP}(\tau)=\frac{1}{N_{\mathrm{snap}}}\sum_{t=1}^{N_{\mathrm{snap}}}\mathrm{PDP}\left(t,\tau\right), \quad (3)$$

where N_{snap} is the number of sampled snapshots.

The multi-sample directional CIR, $h(t,\tau,\Omega_R)$ or $h(t,\tau,\Omega_T)$, can be obtained when the BS deploys an omnidirectional antenna while the UE employs a directional antenna for rotational measurements in this article. The directional antenna acts as a spatial filter for MPCs, capturing MPCs within the HPBW. In the UL, rotating UE directional antenna during channel sounding yields $h(t,\tau,\Omega_T)$, while in the DL, $h(t,\tau,\Omega_R)$ can be obtained. Since the measurement process involves only horizontal rotation of the directional antenna, the resultant angles correspond exclusively to azimuth angles ϕ, namely, the azimuth angle of departure (AAoD) and the azimuth angle of arrival (AAoA). Likewise, the power angular delay profile (PADP) signifies the multipath power distribution over angular and delay domains [29], [30]. In the UL and DL, they can be expressed as

$$\mathrm{PADP}^{\mathrm{U}}\left(\tau,\phi^{\mathrm{AAoD}}\right)=\frac{1}{N_{\mathrm{snap}}}\sum_{t=1}^{N_{\mathrm{snap}}}\left\|h\left(t,\tau,\phi^{\mathrm{AAoD}}\right)\right\|^2,\\ \mathrm{PADP}^{\mathrm{D}}\left(\tau,\phi^{\mathrm{AAoA}}\right)=\frac{1}{N_{\mathrm{snap}}}\sum_{t=1}^{N_{\mathrm{snap}}}\left\|h\left(t,\tau,\phi^{\mathrm{AAoA}}\right)\right\|^2. \quad (4)$$

III. SEGMENTED THRESHOLD DENOISING ALGORITHM

The raw channel measurement data encompasses both thermal noise from the measurement instrument and electromagnetic interference from the surroundings, both of which impinge on the accuracy of channel reciprocity analysis. It is imperative to extract MPCs from the raw data through effective denoising methods. Typically, conventional methods rely on noise thresholds to differentiate between noise and MPCs. Specifically, delay bins exhibiting power levels below the noise

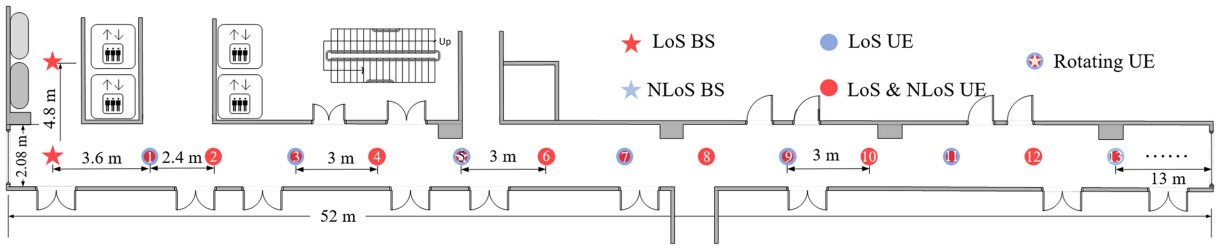

FIGURE 3. Layout of the measurements.

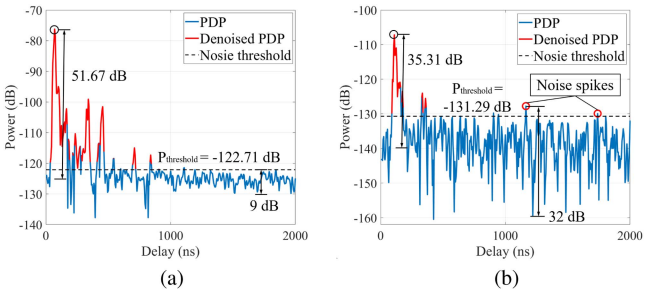

FIGURE 4. Examples of PDP denoising at (a) high SNR and (b) low SNR.

threshold are considered as noise [31]. The noise thresholds are commonly derived through the utilization of the noise floor reference method and peak drop method. Reference [32] investigates several noise floor reference methods and proposes a recommended value that surpasses the mean noise (or noise floor) of the PDP by 6 dB. Additionally, in accordance with ITU-R P.1407-3 [33], a reduction of 20 dB in the peak power of the PDP is regarded as the established noise threshold.

When employing the correlation-based time-domain channel sounder, the noise floor is influenced by factors such as the propagation environment between the TX and RX, the length of the transmitting PN sequence, and the inherent thermal noise of the sounder. As shown in Fig. 4, examples of the APDP are illustrated under high and low SNR conditions, obtained through measurements conducted in LoS and NLoS scenarios. The y-axis "power" refers to the received power relative to the transmitted power, clarifying its unit: dB. Under high SNR conditions, the power difference between the peak power and the noise floor amounts to 51.67 dB. This approximates the correlation gain of the PN sequence ($20\log_{10}(511) \approx 54.17$ dB). In contrast, the power difference between the peak power and the noise floor is only 35.31 dB at low SNR. The noise dynamic range (NDR), which represents the ratio of the maximum and minimum power values of the noise, is approximately 5–10 dB at high SNR. In contrast, it can extend to 25–35 dB at low SNR. It can be broadly understood that the NDR is contingent upon the SNR of the channel. Thus, the noise threshold can't be universally generalized. Additionally, using the noise threshold alone is insufficient for removing noise spikes, as shown in the red dot in Fig. 4.

Algorithm 1: Segmented Threshold Denoising.

Input: The raw APDP P
Output: The denoised APDP $\hat{P}$

Initialize $\hat{P}$ = empty matrix;
// Step 1: Segment APDP
for $1 \le j \le \mathrm{M}$ **do**
  $P^j_{\mathrm{sub}} = [P((j-1)\mathrm{S}+1), \cdots, P(j\mathrm{S})]$;
end
// Step 2: Calculate the noise threshold $\mathrm{P}_{\mathrm{threshold}}$
$J = \arg\min_j(\sum P^j_{\mathrm{sub}})$;
Obtain $\mathrm{P}_{\mathrm{threshold}}$ such that
  $\Pr(P^J_{\mathrm{sub}} \le \mathrm{P}_{\mathrm{threshold}}) = 1-\zeta$;
// Step 3: Assess the effectiveness of each delay bin
for $1 \le j \le \mathrm{M}$ **do**
  $\Phi_j = \{s \mid P^j_{\mathrm{sub}}(s) > \mathrm{P}_{\mathrm{threshold}}\}$;
  $\mathrm{Flag}(j) = \{\mathrm{card}(\Phi_j) \ge \eta\mathrm{S}\}$;
end
$\mathrm{Flag}(\mathrm{M}+1) = \mathrm{True}$;
for $1 \le \tau \le \mathrm{N}$ **do**
  if $\mathrm{Flag}(\lceil \frac{\tau}{\mathrm{S}} \rceil) = \mathrm{True}$ ***and*** $P(\tau) > \mathrm{P}_{\mathrm{threshold}}$ **then**
    $\mathrm{IsEff}(\tau) = \mathrm{True}$;
  else
    $\mathrm{IsEff}(\tau) = \mathrm{False}$;
  end
end
// Step 4: Calculate denoised APDP
$\hat{P} = \mathrm{IsEff} \odot P$;

To address the aforementioned issues, we propose the *Segmented Threshold Denoising* (STDN) algorithm. This algorithm adapts to the NDR for determining the noise threshold and removing noise spikes, as demonstrated in Algorithm 1. In Algorithm 1, N represents the length of the sampling sequence, which is twice the length of the PN sequence and is 1022 in this article. M denotes the number of segments. S represents the number of delay bin samples in each segment, where $\mathrm{S} = \lfloor \mathrm{N}/\mathrm{M} \rfloor$, with $\lfloor\rfloor$ denoting the floor function for rounding down. $\mathrm{P}_{\mathrm{threshold}}$ stands for the noise threshold. ξ represents the noise constant false alarm rate (CFAR), while η indicates the tolerable noise spike ratio. "$\odot$" denotes the Hadamard product.

The APDPs are used for denoising because they can provide an intuitive representation of the characteristics of MPCs and offer reduced complexity compared to using CIR. The APDP can be expressed as follows:

$$P = [\text{APDP}(1), \ldots, \text{APDP}(\tau), \ldots, \text{APDP}(N)]_{1\times \text{N}}. \quad (5)$$

Step 1. Segment APDP: Segmentation plays a crucial role in both determining the noise threshold and removing noise spikes. On the one hand, we obtain pure noise through segmentation. On the other hand, segmentation can be employed to remove noise spikes. We divide the APDP into M segments. After theoretical analysis and experimental validation [34], it is recommended to consider a range of values for segmentation as $[5, \lfloor \text{N}/30 \rfloor]$. In this article, the median within this range, i.e., 20 segments, is selected.

Step 2. Calculate the noise threshold: During the channel measurement, the transmitting sequence is intentionally designed with sufficient length, ensuring the reception of all MPCs. Consequently, the subsequent segments of the received sequence do not contain MPCs, but rather noise. Therefore, we select the segment P^J_{sub} within which the summation of power across all delay bins is minimized, considering it as the representation of pure noise for this measurement.

The real and imaginary parts of the noise are usually assumed as independent Gaussian random variables with zero mean and equal variance, i.e., $X_R, X_I \sim N(0, \sigma^2)$. σ denotes the variance of the distribution. The probability density function (PDF) of noise power (i.e., the square of the noise modulus $|X_R + iX_I|^2$) conforms to an exponential distribution [35]. Unlike conventional methods that employ the noise floor with an added margin as a fixed noise threshold, we adopt the CFAR, a well-known method in radar applications [36], [37], to determine the noise threshold. This method enables the noise threshold to dynamically adjust according to the NDR of the channel measurement data. The probability (i.e., CFAR ξ) of noise power exceeding some level can be derived from the fact that the PDF follows an exponential distribution, and is given by

$$\xi = \exp\left(-\frac{\text{P}_{\text{threshold}}}{2\sigma^2}\right) \quad (6)$$

The noise threshold can be deduced as $\text{P}_{\text{threshold}}[\text{dB}] = 10\log_{10}(-2\sigma^2 \ln(\xi))$. The delay bins with power lower than the noise threshold are considered as noise. This offers interpretability and equity compared to the previous methods. For the measured data, the power at which the cumulative probability of the cumulative distribution function (CDF) of all sampling points in the noise segment P^J_{sub} reaches $1 - \xi$ is considered the noise threshold. To effectively filter out the majority of noise and diminish the likelihood of mistaking low-power multipath as noise, it is recommended to set the CFAR between 1% and 5%. We opt for 1% in this article.

Step 3. Assess the effectiveness of each delay bin: There is no well-established solution to effectively remove noise spikes slightly exceeding the noise threshold. Effectiveness assessment for each segment can address this issue. The two consecutive noise samples are essentially uncorrelated. As a result, larger noise spikes are likely to be present in just one delay bin that surpasses the noise threshold, while samples containing MPCs will likely occupy multiple consecutive delay bins surpassing the noise threshold with a high probability [37]. Consequently, the effectiveness of a segment can be determined by evaluating the ratio of the number of samples surpassing the noise threshold to the total number of samples in that segment. If this ratio is smaller than η, the segment is considered ineffective; otherwise, it is deemed effective. "Effective" indicates the presence of MPCs, while "ineffective" signifies the absence of MPCs within the segment or delay bin. We designate η as 5% in this article. Flag(j) denotes whether the P^j_{sub} is effective. The majority of noise spikes can be removed after segmentation.

Subsequently, the effectiveness of each delay bin in PDP is assessed. A delay bin is considered effective if its power exceeds the noise threshold and the corresponding segment is effective. Otherwise, it is marked as ineffective.

Step 4. Calculate denoised APDP: The denoised APDP can be obtained by performing the Hadamard product between the raw APDP and the vector of effectiveness. The denoised CIR can be calculated as follows:

$$\hat{h}(\tau) = \left[\sqrt{\hat{P}(1)}, \ldots, \sqrt{\hat{P}(\tau)}, \ldots, \sqrt{\hat{P}(N)}\right]_{1\times \text{N}}. \quad (7)$$

Fig. 5 presents examples of denoising results using different methods. In Fig. 5(a) and (b), raising the noise floor of the PDP by 6 dB (the recommended value mentioned above) serves as the noise threshold. At high SNR, MPCs are incorrectly classified as noise, attributed to excessive noise margin. Conversely, at low SNR, noise is erroneously retained as MPCs, owing to the large dynamic range of the noise floor. In Fig. 5(c) and (d), the peak level drops by 35 dB to serve as the noise threshold, a value significantly exceeding the 20 dB stipulated in the ITU recommendation. However, it still misclassifies MPCs as noise under high SNR conditions. In Fig. 5(e) and (f), the STDN algorithm retains all MPCs and removes nearly all noise spikes. We have applied the STDN algorithm to the measured APDPs from various scenarios (indoor and outdoor) and multiple frequency bands (6 GHz band, mmWave, and terahertz). The algorithm consistently distinguishes MPCs from noise, demonstrating its generality. Due to space limitations, we refrain from listing the results in detail here. This STDN algorithm provides a solid foundation for equitable reciprocal analysis.

IV. CHANNEL RECIPROCITY ANALYSIS

In this section, a comprehensive analysis of the reciprocity between the UL and DL channels in TDD/FDD systems is conducted from four perspectives: path loss, delay spread, correlation coefficient, and multipath power differences.

A. PATH LOSS

Path loss is a vital parameter associated with large-scale fading, and it significantly impacts the coverage performance of

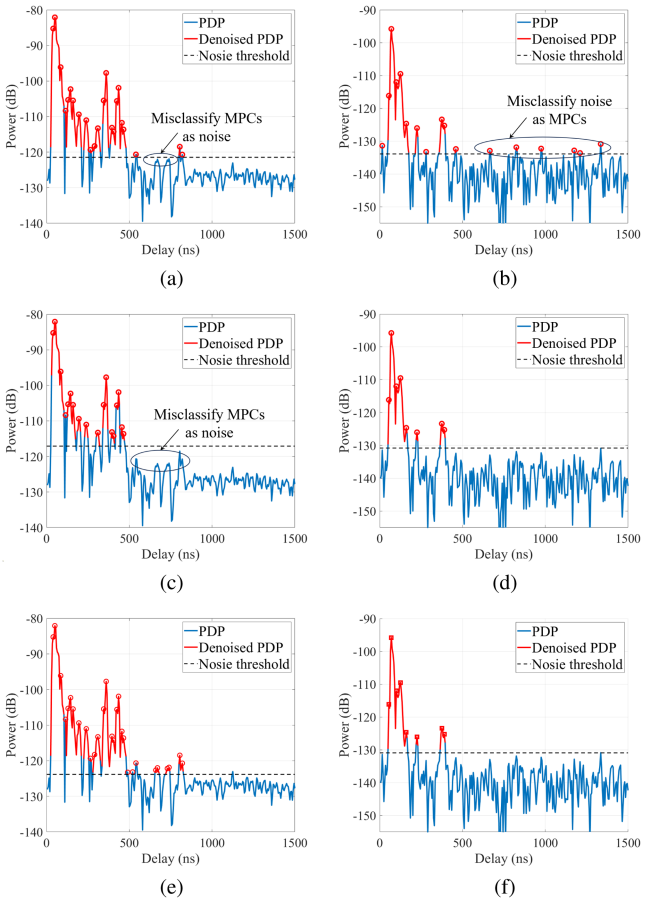

FIGURE 5. Comparative examples of three denoising methods at high and low SNR. (a) The noise floor reference method at high SNR. (b) The noise floor reference method at low SNR. (c) The peak drop method at high SNR. (d) The peak drop method at low SNR. (e) The STDN algorithm at high SNR. (f) The STDN algorithm at low SNR.

radio communication systems. Currently, two prevalent path loss models are the floating intercept (FI) model and the close-in (CI) free space reference distance model. The FI model finds extensive application in the 3 rd Generation Partnership Project (3GPP) and WINNER II channel models [38], [39], providing the most accurate fit to collected measurement data with minimum mean square error (MMSE). The FI model can be expressed as [40]

$$\mathrm{P\,L_{FI}}(d)[\mathrm{dB}] = \alpha_{\mathrm{FI}} + 10\beta_{\mathrm{FI}}\log_{10} d + X_{\sigma}^{\mathrm{FI}}, \tag{8}$$

where P L denotes the path loss in dB as a function of the 3D distance d between TX and RX, α_{FI} is a floating intercept in dB, β_{FI} denotes the linear slope. X_{σ}^{FI} is the zero-mean log-normal random variable with standard derivation σ to model shadow fading. The CI model is derived by applying a constraint anchor point at the close-in reference distance d_0 during the process of fitting the best-fit line based on the MMSE criterion. The CI model incorporates a parameter associated with free space propagation, thereby providing physical insight into channel propagation characteristics [41]. It can be

TABLE 2. Parameters of the Path Loss Models and RMS Delay Spread Model

Scenarios	f (GHz)	Link	Path loss			RMS delay spread*
			FI		CI	
			α_{FI} (dB)	β_{FI}	n	μ (ns)
LOS	6	DL	48.08	1.79	1.79	40.74
		UL	48.75	1.75	1.81	40.74
	6.5	DL	54.87	1.80	2.26	38.02
		UL	54.04	1.85	2.26	37.15
	7	DL	54.87	1.50	2.30	31.62
		UL	54.04	1.56	2.29	30.90
	7.5	DL	65.87	1.30	2.51	37.15
		UL	64.74	1.39	2.51	37.15
NLOS	6	DL	61.31	2.46	3.45	32.36
		UL	62.06	2.43	3.48	32.36
	6.5	DL	67.87	2.44	3.88	31.63
		UL	70.78	2.22	3.87	31.63
	7	DL	70.50	2.68	4.26	48.98
		UL	71.44	2.57	4.23	45.71
	7.5	DL	78.78	2.15	4.51	51.29
		UL	83.39	2.08	4.59	50.12

* μ denotes the mean for the log-normal distribution fit of RMS delay spreads, measured in nanoseconds (ns).

expressed as

$$\mathrm{PL_{CI}}(f, d)[\mathrm{dB}] = \mathrm{FSPL}(f, 1m)[\mathrm{dB}] + 10n\log_{10}(d) + X_{\sigma}^{\mathrm{CI}}, \tag{9}$$

where n denotes the path loss exponent (PLE), and $\mathrm{FSPL}(f, 1m)$ denotes the free space path loss in dB at a TX-RX separation distance of 1 m for the carrier frequency f, i.e.,

$$\mathrm{FSPL}(f, 1m)[\mathrm{dB}] = 20\log_{10}\left(\frac{4\pi f}{c}\right), \tag{10}$$

where c is the speed of light. X_{σ}^{CI} is the log-normal random variable with 0 dB mean and standard deviation σ [42].

The parameters fitted by the FI model and the CI model are presented in Table 2. The linear slope β_{FI} for the FI model is less than 2 in LoS scenarios and ranges between 2 and 3 in NLoS scenarios. The PLE n for the CI model is less than 3 in LoS scenarios and greater than 3 in NLoS scenarios. Within the same scenario, as the frequency increases, the PLE becomes larger. It is apparent that the parameters fitted for UL and DL are approximately equal in TDD systems, whether it is the FI model or the CI model. This aligns with the findings of [43], which concluded that the path loss for the UL and DL is nearly identical in suburban environments when using a carrier frequency of 915 MHz. In FDD systems, there are large differences in the fitted parameters between UL and DL, with PLE differences of up to 1.

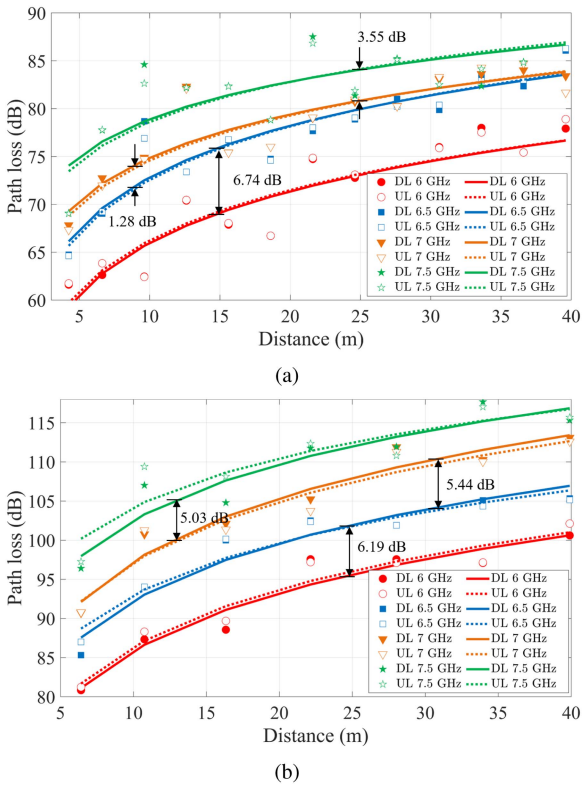

FIGURE 6. Path loss and FI model fitting results in (a) LoS scenario, and (b) NLoS scenario. The markers represent the measured path loss. The lines correspond to the path loss fitting results of the FI model.

The fitted result figures provide a more intuitive representation of these differences. In Fig. 6, we illustrate the fitted results of the path loss model for both the UL and DL in TDD/FDD systems. Due to the similarity in the fitting curves between the CI model and the FI model, the figures for the CI model are not provided. In TDD systems, it is observed that the fitting curves for both UL and DL exhibit only slight differences in the LoS/NLoS scenario, typically less than 1 dB. However, substantial differences in path loss emerge between UL and DL in FDD systems. Specifically, for the frequency pair of 6 and 6.5 GHz, the average path loss differences are 6.74 dB in the LoS scenario and 6.19 dB in the NLoS scenario. Meanwhile, for the 6.5 and 7 GHz frequency pair, the average path loss difference in the LoS scenario is 1.28 dB at short distances, with virtually no discernible difference at longer distances. Whereas in the NLoS scenario, the differences reach up to 5.44 dB. For the 7 and 7.5 GHz frequency pair, the average path loss differences are 3.55 dB in the LoS scenario and 5.03 dB in the NLoS scenario. In the case of the farthest frequency pair, 6 and 7.5 GHz, the average path loss differences in LoS and NLoS scenarios are notably substantial, measuring 11.57 dB and 16.66 dB, respectively. Table 3 presents the differences in path loss between different frequency bands, encompassing both the FI and CI models. It is evident that the results from the two models exhibit differences of less than 1 dB, affirming the reliability of the conclusions and demonstrating their independence from the fitting model.

TABLE 3. Differences in Path Loss Between Different Frequency Bands

Differences (dB)	Fitting model	6.5 - 6 GHz	7 - 6.5 GHz	7.5 - 7 GHz
LoS	FI	6.74	1.28	3.55
	CI	6.45	1.07	3.28
NLoS	FI	6.19	5.44	5.03
	CI	5.91	5.39	4.64

These significant path loss differences have the potential to transform a previously reliable communication link into one of poor quality. Consequently, when designing FDD systems, it becomes imperative to take into account the coverage range of distinct frequency bands for both the UL and DL.

B. DELAY SPREAD

RMS delay spread τ_{RMS} is defined as the square root of the second central moment of APDP and is widely used to characterize the delay dispersion of channels [44]. Next, we delve into the reciprocity of RMS delay spread between the UL and DL in TDD/FDD systems. The RMS delay spread is calculated as

$$\tau_{\text{RMS}} = \sqrt{\frac{\sum_{l=1}^{L} (\tau_l - \tau_{mean})^2 P(\tau_l)}{\sum_{l=1}^{N} P(\tau_l)}}, \tag{11}$$

where τ_l and $P(\tau_l)$ denote the delay and power of the lth path, respectively. τ_{mean} is the average delay spread and can be mathematically expressed as

$$\tau_{\text{mean}} = \frac{\sum_{\tau=1}^{L} \tau_l P(\tau_l)}{\sum_{l=1}^{L} P(\tau_l)}. \tag{12}$$

The measured RMS delay spreads follow a log-normal distribution. Fig. 7 illustrates the CDFs of the log-normal distribution fitting for RMS delay spread. This distribution has been extensively used in fitting RMS delay spreads, not only in the 3GPP channel model but also in other literature [38], [44]. It can be observed that the fitted curves of the UL and DL are almost perfectly matched, displaying a consistent trend in TDD systems. In FDD systems, slight differences are present among all frequency pairs in LoS scenarios. However, in NLoS scenarios, the fitted curves are closer for the 6 and 6.5 GHz frequency pair, as well as the 7 and 7.5 GHz frequency pair, while the other frequency pairs exhibit discernible differences. The mean values of the log-normal distribution fitting for the RMS delay spread in the UL and DL of TDD/FDD systems are presented in Table 2. The maximum difference in RMS delay spread is observed to be 9.84 ns in the LoS scenario and 19.66 ns in the NLoS scenario.

Reference [14] analyzes the reciprocity of RMS delay spread in outdoor-to-indoor (O2I) and indoor-to-outdoor (I2O) scenarios. In the O2I scenario, the mean RMS delay

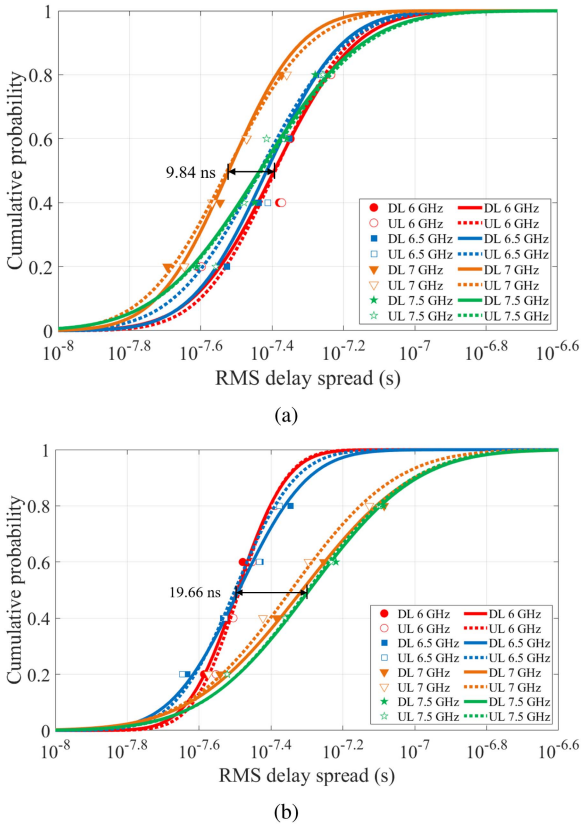

FIGURE 7. CDFs of the log-normal fit for the measured RMS delay spreads in (a) LoS scenario, and (b) NLoS scenario. The markers represent the measured RMS delay spreads (only 20%, 40%, 60%, and 80% points are plotted). The lines represent the CDFs of the log-normal distribution fitting for RMS delay spreads.

spread is 40 ns, while in I2O scenarios, it is 34 ns. This contradicts the nearly identical RMS delay spread observed in our TDD systems for both UL and DL. The reason for this difference lies in its focus on exploring the channel characteristics between independently measured O2I and I2O scenarios, without a strict differentiation between UL and DL. Additionally, ref. [18] points out a delay differential ranging from several to a dozen nanoseconds in the urban macrocellular scenario of FDD systems, where the UL carrier frequency is 1.8 GHz, and the DL carrier frequency is 1.9 GHz. This corresponds with the conclusion drawn in this article regarding the presence of RMS delay spread differences between UL and DL in FDD systems. The RMS delay spread findings offer valuable insights for designing the guard interval or cyclic prefix of orthogonal frequency-division multiplexing technology in FDD systems [45].

C. CORRELATION COEFFICIENT

It is crucial to explore whether there is a correlation between UL and DL channels in TDD/FDD systems. If such a correlation does exist, it may be feasible to extract common components from the estimated CSI of the UL for utilization in DL channel estimation. This could result in significant reductions in pilot overhead. The correlation coefficient serves as a metric for quantifying the degree of linear association between two random variables. Consequently, it can be utilized to assess the reciprocity between the UL and DL channels in terms of multipath distribution, shedding light on the inherent relationship between the UL and DL. Therefore, the well-known pearson correlation coefficient (PCC) is applied to calculate the correlation between the denoised CIR of the UL and DL. A higher correlation is indicated by a larger absolute value of the correlation coefficient, approaching 1. The formula for calculating the correlation coefficient is as follows:

$$\rho_{\mathrm{PCC}}\left(\hat{h}_{\mathrm{U}}, \hat{h}_{\mathrm{D}}\right) = \frac{\mathbb{E}\left\{\hat{h}_{\mathrm{U}}\hat{h}_{\mathrm{D}}\right\} - \mathbb{E}\left\{\hat{h}_{\mathrm{U}}\right\}\mathbb{E}\left\{\hat{h}_{\mathrm{D}}\right\}}{\sqrt{\mathbb{E}\left(\hat{h}_{\mathrm{U}}^2\right) - \mathbb{E}^2\left(\hat{h}_{\mathrm{U}}\right)}\sqrt{\mathbb{E}\left(\hat{h}_{\mathrm{D}}^2\right) - \mathbb{E}^2\left(\hat{h}_{\mathrm{D}}\right)}}, \tag{13}$$

where $\mathbb{E}$ denotes the expectation operation, and $\hat{h}_{\mathrm{U}}$ and $\hat{h}_{\mathrm{D}}$ respectively represent the denoised CIR for the UL and DL. The PCC quantifies the channel correlation between UL and DL in the delay domain, treating the multipath channel as a sequence and only assessing the numerical similarity between MPCs, while disregarding the physical significance of these channel MPCs. Furthermore, when calculating similarity using PCC, MPCs with lower power are often overlooked. From the perspective of radio wave propagation, the scattering objects in the propagation environment determine the arrival of multipath in the form of clusters at the RX [46]. Therefore, we introduce the concept of clusters to compute the correlation coefficient, referred to as cluster-based correlation coefficient (CBCC). This metric overcomes the limitations of PCC in terms of lacking physical meaning and disregarding low-power MPCs.

Saleh and Valenzuela have established the widely adopted Saleh Valenzuela (SV) clustering model in the delay domain of wideband channels [47]. The SV model is founded on a doubly stochastic Poisson process. Accordingly, the expression for the CIR in (1) is replaced by[1] [48]:

$$h(\tau) = \sum_{k=1}^{K}\sum_{l=1}^{L_k}\beta_{lk}e^{j\phi_{lk}}\delta\left(\tau - T_k - \tau_{lk}\right), \tag{14}$$

where the arrival delay of the kth cluster is denoted as T_k. τ_{lk} represents the excess arrival delay of the lth path within the kth cluster, measured from the beginning of the cluster. Its phase is denoted by ϕ_{lk}. The variables K and L_k correspond to the maximum number of clusters and the maximum number of paths in the k-th cluster, respectively. Additionally, the amplitude of the lth path in the kth cluster is denoted as β_{lk}, and its mean square value, $\overline{\beta_{lk}^2}$, can be derived from:

$$\overline{\beta_{lk}^2} = \overline{\beta_{00}^2}e^{-T_k/\Gamma}e^{-\tau_{lk}/\kappa}, \tag{15}$$

[1]Since it is a single-sample sampling, the parameter t can be disregarded. Furthermore, in wideband single-antenna measurements, it is not possible to discern the angle of multipath, hence the parameters Ω_T and Ω_R can also be omitted.

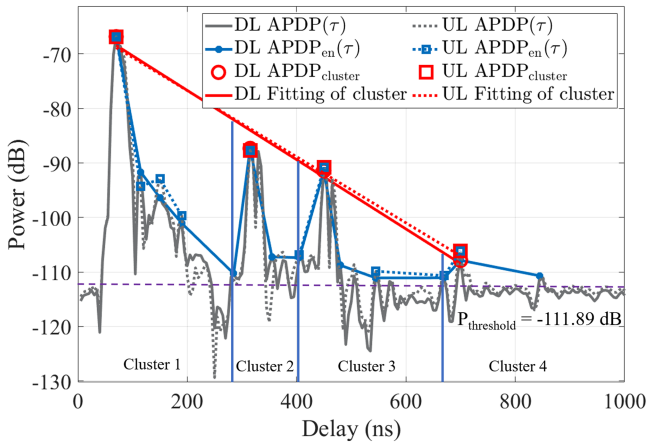

FIGURE 8. Illustration of clustering with SV model for the 6th point in LoS scenario at 6 GHz.

where $\overline{\beta_{00}^2}$ denotes the average gain of the first path in the initial cluster. $1/\Gamma$ and $1/\kappa$ denote the power decay factors of the cluster and path, respectively. Specifically, the UL and DL APDPs are clustered with the 'Bubbling' algorithm according to the following two criteria: first, the power arriving of the first path in each cluster is monotonically decreasing along with the delay; second, the power of the first path in each cluster is the local maximum in APDP. The detailed clustering steps refer to the literature [49]. The SV model clustering is illustrated in Fig. 8, where the black lines represent the APDPs, and the blue lines denote the envelope formed by the local maxima of the APDPs, expressed as $\mathrm{PDP}_{\mathrm{en}}(\tau)$. Subsequently, the two criteria of the SV model are employed to identify the first arrival path in the cluster, marked as red circles and squares for DL and UL respectively. It can be observed that the entire CIR has been divided into four clusters. The point of minimum value in the $\mathrm{PDP}_{\mathrm{en}}$ between two clusters is considered as the inter-cluster separation point. Furthermore, the power of the cluster is exponentially fitted and is depicted by the red line.

Therefore, the CBCC can be derived by computing the PCC from the respective clusters, followed by power weighting. The formula is expressed as follows:

$$\rho_{\mathrm{CBCC}} = \sum_{k=1}^{K} \frac{w_{\mathrm{U}}^k + w_{\mathrm{D}}^k}{2} \rho_{\mathrm{PCC}} \left(\hat{h}_{\mathrm{U}}^k, \hat{h}_{\mathrm{D}}^k \right),$$

$$w^k = \frac{\lg\left(\overline{\beta_{0k}^2}/\mathrm{P}_{\mathrm{threshold}}\right)}{\lg\left(\prod_{k=1}^{K}\left(\overline{\beta_{0k}^2}/\mathrm{P}_{\mathrm{threshold}}\right)\right)}, \tag{16}$$

where w^k denotes the weight of the power of the kth cluster relative to the total channel power, with UL and DL weights being averaged in the CBCC computation. The weight is determined by the initial path power of each cluster and is related to the cluster power decay factor. $\hat{h}_{\mathrm{U/D}}^k$ denotes the denoised CIR of the kth cluster, acquired by intercepting the CIR of the corresponding segment.

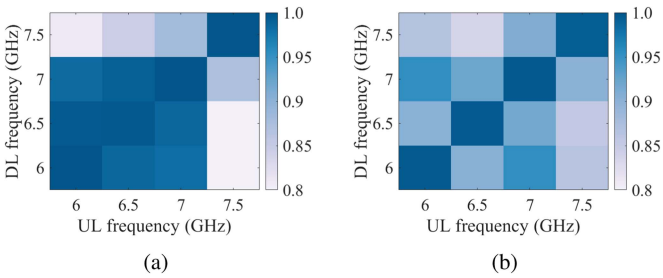

FIGURE 9. Correlation coefficient between the UL and DL channels at the 6th measurement point. (a) PCCs. (b) CBCCs.

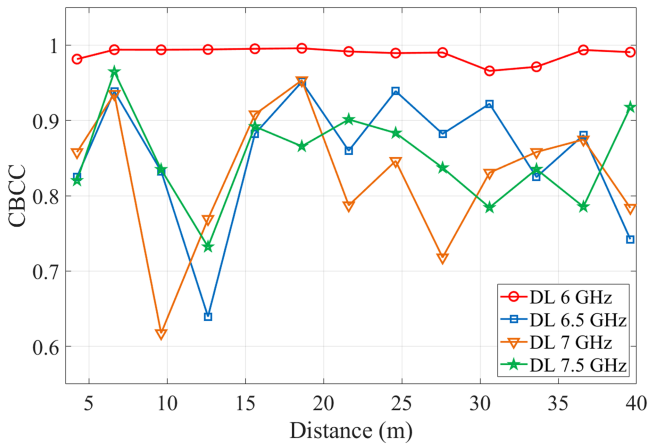

FIGURE 10. CBCCs for all measurement points in the UL channel with a center frequency of 6 GHz, and the DL channels at frequencies of 6, 6.5, 7, and 7.5 GHz.

First, an analysis of the advantages of CBCC over PCC is conducted. Fig. 9 illustrates the PCCs and CBCCs between the UL and DL, with the 6th measurement point as a representative example. It can be observed that PCCs and CBCCs exhibit certain similarities. For example, in TDD systems, along the diagonal, the correlation is very high, exceeding 95%. In FDD systems, the correlation coefficients mostly exceed 80%. The correlation coefficient results exhibit diagonal symmetry, which aligns with our expectation that the coefficients remain almost unchanged when swapping UL and DL frequency bands. However, PCCs tend to approach two extremes, either very close to 1 or relatively close to 80%. This susceptibility arises from the influence of extreme values, particularly LoS paths, causing them to overlook the overall channel similarity. The CBCC surmounts this limitation in correlation assessment by introducing the concept of clusters.

Then, we explore the distance dependence of the CBCCs. Since the DL frequency band is typically higher than the UL frequency band in FDD systems, we select the UL frequency band as 6 GHz and DL frequency bands as 6, 6.5, 7, and 7.5 GHz for analysis, as illustrated in Fig. 10. It is evident that in TDD system, a robust correlation exists between the UL and DL channels across all measurement points, with all values exceeding 95%. In FDD systems, the correlation exhibits a

TABLE 4. CBCCs for Each Frequency Pair in Both LoS and NLoS Scenarios

CBCCs	UL / DL	6 GHz	6.5 GHz	7 GHz	7.5 GHz
LoS	6 GHz	99.14%	86.97%	83.37%	84.52%
	6.5 GHz	88.04%	98.08%	86.34%	85.15%
	7 GHz	84.61%	86.00%	98.38%	85.73%
	7.5 GHz	83.71%	85.89%	89.24%	99.15%
NLoS	6 GHz	97.12%	77.33%	82.06%	80.81%
	6.5 GHz	79.34%	98.37%	85.95%	89.36%
	7 GHz	80.25%	88.01%	98.14%	90.28%
	7.5 GHz	85.48%	85.57%	89.63%	98.31%

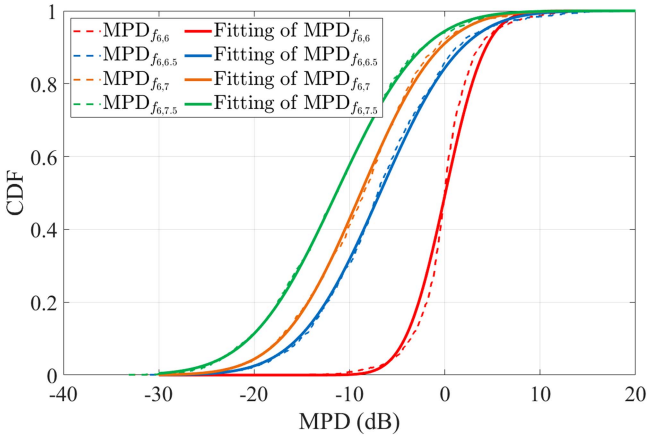

FIGURE 11. CDFs of MPD$_{6,f_D}$ and their results fitted with a normal distribution.

fluctuating trend without apparent distance dependence. However, the CBCCs display a scene-specific relationship. For instance, locations with L-shaped corridors, such as the 2nd, 5th, and 8th measurement points, exhibit strong correlations for all frequency pairs. Conversely, at the 4th measurement point, the correlations for all frequency pairs are comparatively low. This could be attributed to variations in scatterers around distinct measurement points, significant differences in the frequency-dependent electromagnetic properties of these scatterers, and consequently resulting in disparities in the MPCs distribution. Similar characteristics are also observed in other frequency bands and in NLoS scenarios, which are not reiterated here.

Finally, we investigate the correlation of channels for various frequency pairs in indoor corridor scenarios. The median of the CDF for CBCCs across all measurement points within a frequency pair is considered the CBCCs of this scenario. The CBCCs in LoS and NLoS scenarios are summarized in Table 4. The values along the diagonal in the table represent the correlation coefficients for TDD systems, while those in the lower triangle pertain to FDD systems. The CBCCs for TDD systems consistently surpass those of FDD systems, with values exceeding 98% for nearly all frequency pairs, regardless of LoS or NLoS scenarios. Conversely, in FDD systems, the CBCCs for most frequency pairs tend to hover around 80% to 90%. This suggests that FDD systems still maintain a relatively robust correlation between the UL and DL channels. This can be attributed to the fact that, even though the UL and DL operate in different frequency bands, the propagation characteristics of electromagnetic waves are influenced by the same physical environment, and the mapping relationship between the MPCs and the surrounding scatterers is inherent. Additionally, as the frequency interval between UL and DL increases, the correlation tends to slightly decrease.

Therefore, in TDD systems, the UL and DL channels exhibit nearly perfect correlation, both in LoS and NLoS scenarios. In FDD systems, the UL and DL channels demonstrate partial similarity. Despite sharing the same physical propagation environments, resulting in a correlation exceeding 80%, there is still a loss of correlation due to differences in frequency bands of the UL and DL. This could be attributed to discrepancies in the power and distribution of MPCs between the UL and DL.

D. MULTIPATH POWER DISSIMILARITY

The correlation coefficient normalizes the CIR during the calculation process, without taking into account the difference in multipath power between the UL and DL channels. Therefore, a metric is proposed, referred to as MPD, to assess this difference. Following this, the channel reciprocity of the UL and DL will be discussed in terms of the power difference between MPCs. To assess the power differential of MPCs between the UL and DL, we propose a metric distinct from the large-scale path loss model, referred to as MPD. Due to the high delay resolution of the measured CIR, the power corresponding to each effective delay bin can be regarded as the power of a propagation path. Consequently, it allows for a direct analysis of the multipath power differences between the UL and DL channels from the perspective of delay bins. MPD can be expressed as follows:

$$\mathrm{MPD}_{f_\mathrm{U},f_\mathrm{D}}[\mathrm{dB}] = 10\lg\frac{P_{i,f_\mathrm{D}}(\tau_l)}{P_{i,f_\mathrm{U}}(\tau_l)}, \tag{17}$$

where $\mathrm{MPD}_{f_\mathrm{U},f_\mathrm{D}}$ represents the power differences among MPCs when the UL frequency is f_U and the DL frequency is f_D. $P_{i,f_{\mathrm{U/D}}}(\tau_l)$ denotes the power of the lth path at the ith measurement point when the UL/DL frequency is $f_\mathrm{U}/f_\mathrm{D}$. In the LoS scenario, the range of values for i is from 1 to 13, while in the NLoS scenario, it ranges from 1 to 7.

The CDFs of $\mathrm{MPD}_{f_\mathrm{U},f_\mathrm{D}}$ for different frequency pairs, along with their fitted normal distribution results, are depicted in Fig. 11. Only the CDF curves of MPD with UL center frequency at 6 GHz and DL center frequencies at 6, 6.5, 7, and 7.5 GHz are provided, serving as representations of the disparity in MPD across different frequency intervals. The

TABLE 5. Mean μ and Variance σ Results of MPD Normal Distribution Fitting in LoS and NLoS Scenarios

MPD	UL / DL	6 GHz		6.5 GHz		7 GHz		7.5 GHz	
	Parameter	μ	σ	μ	σ	μ	σ	μ	σ
LoS	6 GHz	-0.06	3.33	6.58	6.75	9.01	6.85	11.98	7.18
	6.5 GHz	-6.79	6.74	-0.27	3.50	2.16	6.77	5.13	6.83
	7 GHz	-8.82	6.82	-2.30	6.80	0.14	3.21	3.11	6.46
	7.5 GHz	-11.38	7.15	-4.86	6.72	-2.43	6.58	0.35	3.32
NLoS	6 GHz	0.31	2.72	6.39	5.80	6.69	6.67	10.17	7.18
	6.5 GHz	-5.46	5.73	0.62	2.21	0.92	4.80	4.40	4.73
	7 GHz	-6.33	6.88	-0.25	5.26	0.06	2.01	3.54	3.65
	7.5 GHz	-9.07	7.06	-2.99	5.03	-2.68	3.74	0.80	1.88

fitting results of the normal distribution for $\mathrm{MPD}_{f_\mathrm{U},f_\mathrm{D}}$ across different frequency pairs are presented in Table 5, providing the respective fitted mean (μ) and variance (σ). A larger absolute value of μ indicates a greater disparity in multipath power between the UL and DL.

It is evident that in TDD systems, the mean values of MPD tend to approach zero, indicating a near equivalence in power between UL and DL MPCs. In FDD systems, as the UL and DL frequency interval expands, the absolute values of the mean within the normal distribution of MPD increase. This aligns with the principle of signal propagation in free space, where a wider frequency interval leads to greater dissimilarity in single-path power.

In the LoS scenario of TDD systems, the variance of the MPD normal distribution fitting falls between 3 and 3.5. In contrast, for FDD systems, the variance is significantly larger than that of TDD systems, ranging from 6 to 7.5. This indicates that different frequency bands in the UL and DL of FDD systems result in a more pronounced dispersion in MPD. Furthermore, the variance tends to slightly increase with the widening of the frequency interval. This suggests that increasing the frequency interval between UL and DL also leads to a more dispersed MPD. In the NLoS scenario, the dependency relationship between the mean and variance of MPD with frequency interval mirrors that of the LoS scenario. However, compared to the LoS scenario, the mean and variance of MPD in the NLoS scenario are generally slightly smaller. For instance, in most frequency pairs, the absolute value of the mean MPD in the NLoS scenario is less than that in the LoS scenario. In TDD systems, the range of MPD variance is between 1.5 and 3. Compared to the majority being LoS paths and low-order reflection paths in LoS scenarios, most MPCs in NLoS scenarios are high-order reflections. These high-order reflection MPCs tend to diminish the disparity in multipath power, resulting in a more concentrated distribution of MPD.

Subsequently, we will delineate the observed trend of the mean of MPD increasing with larger frequency intervals. However, the same frequency interval does not yield the same MPD values, as they also vary with the center frequency. For instance, in the cases of frequency pair 6 and 6.5 GHz, as well as 6.5 and 7 GHz, both with a frequency interval of 0.5 GHz, their respective MPD are -6.79 and -2.30 dB. We draw inspiration from the calculation method for LoS path power in free-space propagation to model the relationship between MPD and center frequency, as well as frequency interval. When the transmit power and the gains of the transmit and receive antennas are normalized, the gain of the free-space path is given by:

$$P_\mathrm{Gain} = \left(\frac{c}{4\pi df}\right)^2, \tag{18}$$

where P_Gain denotes the path gain. Therefore, the MPD for the LoS path can be expressed as:

$$\mathrm{MPD}_\mathrm{LoS}[\mathrm{dB}] = 10\log_{10}\left(\frac{P^\mathrm{D}_\mathrm{Gain}}{P^\mathrm{U}_\mathrm{Gain}}\right) = 20\log_{10}\left(\frac{f_\mathrm{U}}{f_\mathrm{D}}\right), \tag{19}$$

where $P^\mathrm{U}_\mathrm{Gain}$ and $P^\mathrm{D}_\mathrm{Gain}$ represent the gain of the LoS path for the UL and DL, respectively. Letting $\Delta f = f_\mathrm{D} - f_\mathrm{U}$, the $\mathrm{MPD}_\mathrm{LoS}$ can be expressed as:

$$\mathrm{MPD}_\mathrm{LoS}[\mathrm{dB}] = 20\log_{10}\left(1 - \frac{\Delta f}{f_\mathrm{D}}\right). \tag{20}$$

Hence, the fitting equation for MPD can be formulated as:

$$\mathrm{MPD}[\mathrm{dB}] = 20\gamma\log_{10}\left(1 - \frac{\Delta f}{f_\mathrm{D}}\right), \tag{21}$$

where γ denotes the MPD dependency factor. The fitting results for the mean values of MPD in the LoS scenario are shown in Fig. 12. As anticipated, the combined effect of all MPCs leads to a significantly larger MPD (in absolute value) compared to the MPD of the LoS path alone. This phenomenon is attributed to the presence of abundant reflection and scattering paths in the 6 GHz band. In LoS and NLoS scenarios, the values of γ are 5.81 and 4.59 respectively. This indicates that in the NLoS scenario, the power difference of MPCs between the UL and DL channels is diminished.

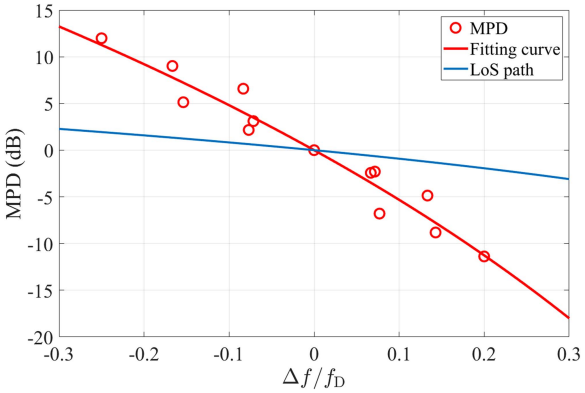

FIGURE 12. Relationship between MPDs and frequency interval, center frequency in LoS scenario.

Therefore, in TDD systems, the power of MPCs in both the UL and DL channels is nearly identical. In FDD systems, there exists a disparity in the power of MPCs between the UL and DL channels, which demonstrates dependence on center frequency and frequency interval. A model has been established to describe this relationship. If the multipath power is known for a specific DL frequency band, one can extrapolate the corresponding multipath power for the UL frequency band using the MPD model. Vice versa.

In summary, based on the analysis of path loss, delay spread, correlation coefficient, and multipath power differences between the UL and DL channels, it can be concluded that TDD systems are nearly perfectly reciprocal, whereas FDD systems exhibit partial reciprocity.

V. INFLUENTIAL FACTORS OF RECIPROCITY

As previously discussed, the conclusion has been drawn regarding the partial reciprocity of the UL and DL channels in the FDD systems. This partial reciprocity can be attributed to the complex propagation of MPCs. Therefore, further analysis of multipath parameters such as power, delay, angle, etc., as well as the propagation process of MPCs, can be conducted to assess the factors influencing their reciprocity.

However, it is challenging to extract these parameters and determine the propagation trajectories of MPCs from existing measurement data. Therefore, the ray-tracing approach is introduced to obtain this information. The ray-tracing approach provides a description of all propagation paths from the TX to the RX in terms of rays. This method furnishes channel parameters of MPCs, including power, delay, AoA, and AoD, allowing for an accurate reflection of the scenario's influence on the channel [50]. The commercial ray-tracing tool, Wireless InSite [51], developed by Remcom, is utilized in the simulations. It is worth noting that the accuracy of multipath power in ray-tracing simulation results is constrained by the electromagnetic properties of the environmental materials. Therefore, simulations can be conducted in a specific frequency band to characterize the propagation paths of MPCs while overlooking differences in multipath power.

In the ray-tracing simulation, MPCs are allowed to propagate through direct, reflected, or diffracted paths. These propagation mechanisms are relatively straightforward, relying on established electromagnetic propagation theories such as geometrical optics and geometrical theory of diffraction. They do not rely on complex propagation models or model parameters, resulting in more realistic and reliable MPCs. This is in contrast to diffuse scattering, which involves multiple propagation models, is comparatively complex, and heavily depends on model parameters [52]. As shown in Fig. 13, ray-tracing simulations at 6 GHz are conducted within the same indoor corridor scenario. A few representative MPCs are highlighted, including the LoS path, as well as the first and second-order reflective MPCs originating from the side walls and floor-to-ceiling windows. The relation of the identified MPCs with the geometric layout of the scenario is also depicted. Paths 2–5 correspond to the first, second, and third-order reflected paths caused by the floor-to-ceiling windows located behind the TX and RX. The following will separately discuss the influencing factors of reciprocity from the perspectives of multipath delay and angle.

A. MULTIPATH DELAY

The APDPs allow us to observe the reciprocity between UL and DL channels from the perspective of the delay-domain distribution of MPCs. As shown in Fig. 14(a), we analyze the difference between denoised APDPs measured in UL and DL across various frequency bands, taking the 6th measurement point as an example. In TDD systems, the APDPs of UL and DL are almost identical. Consequently, further investigation into the reciprocity of UL and DL in FDD systems primarily involves scrutinizing the distinctions introduced by different frequency bands. In FDD systems, the APDPs of UL and DL demonstrate roughly parallel trends. The majority of MPCs appear in the same delay bins for all frequency bands, which we term "public MPCs". These public MPCs exhibit consistent peak trends, except for differences in path power, as indicated by the ovals. The observed power differences can be attributed to the inconsistent attenuation characteristics of UL and DL in free space, as well as the distinct electromagnetic properties of environmental materials across varying frequency bands. In addition, a minority of MPCs are only observable in specific frequency bands, denoted as "private MPCs" and marked by the rectangle. For instance, MPCs are exclusively present at 6.5 and 7.5 GHz around 270 ns. This is due to the limited delay resolution, where multiple MPCs with similar delays are superimposed in the same delay bin. In some bands, this results in constructive interference, while in others, it leads to destructive interference.

Upon comparing the simulated PDP with the measured APDPs, it is evident that the ray-tracing simulation results only capture partial public MPCs, without private MPCs, as illustrated in Fig. 14(b). These public MPCs encompass the LoS path and low-order strong reflection paths. The four peaks at 305 and 440 ns respectively arise from the first, second, and

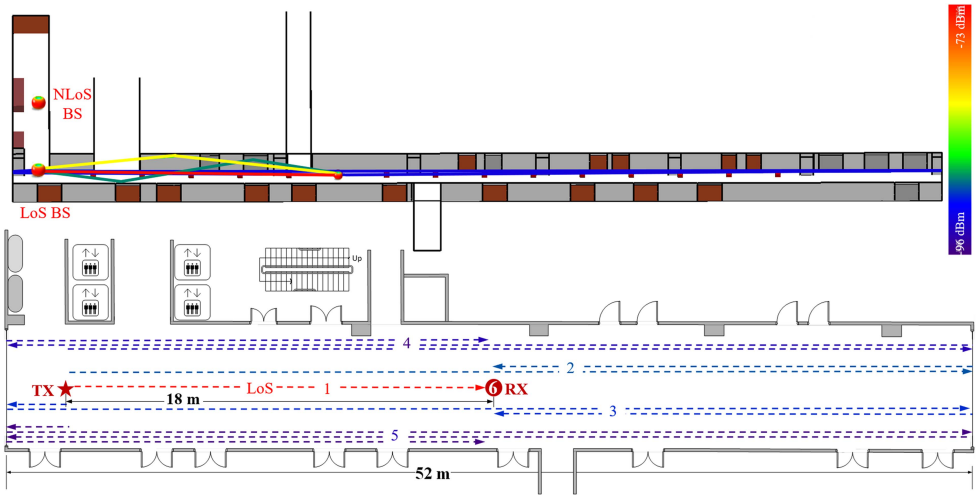

FIGURE 13. Ray-tracing simulation in the corridor scenario and the relation of the identified MPCs with the geometric layout of the scenario at the 6th measurement point.

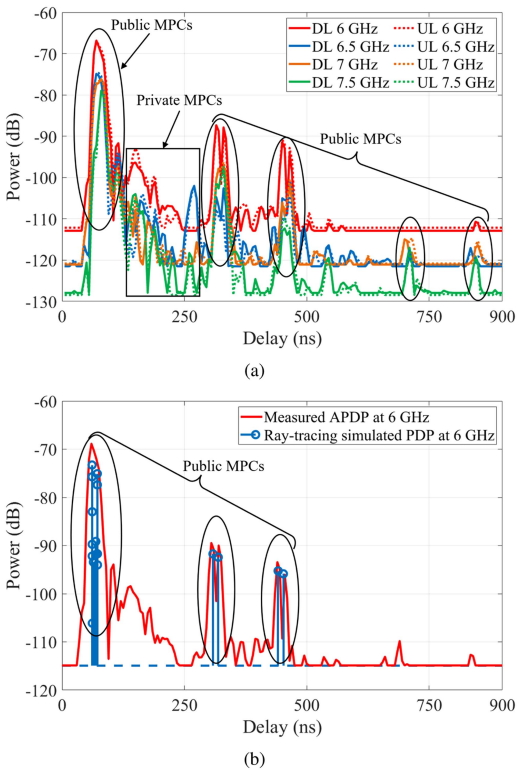

FIGURE 14. APDPs at the 6th measurement point in the LoS scenario. (a) The measured multi-frequency APDPs of the UL and DL. (b) The ray-tracing simulated PDP at 6 GHz. The public MPCs and private MPCs are labeled.

third-order reflections of the floor-to-ceiling windows, corresponding to paths 2–5 in Fig. 13. Therefore, we can deduce that the public MPCs comprise the LoS path and the low-order reflection paths. Furthermore, an average of over 85% of the total path power is contributed by the public MPCs. As a result, the public MPCs play a dominant role, and the private MPCs can be completely ignored in certain studies.

Regarding the private MPCs, we draw the following conclusion. By aligning the ray-tracing results with the propagation delay, it is inferred that the private MPCs likely stem from higher-order reflections or diffuse scattering from the sidewalls. This inference arises from the fact that the delay of private MPCs lies between the delay of the forward low-order reflections and the first-order reflection of the rear floor-to-ceiling window. Other propagation mechanisms are highly unlikely to generate MPCs at this specific delay. Reference [53] supports our viewpoint, highlighting the significant variation in diffuse scattering multipath power with frequency. Additionally, this also explains the relatively strong power of MPCs at a delay of 270 ns in both the 6.5 and 7.5 GHz frequency bands. This occurrence is attributed to the fact that the power of diffuse scattering MPCs fluctuates erratically with frequency, with notable gain occurring only in specific frequency bands without clear frequency dependence.

B. MULTIPATH ANGLE

The research will be further extended to the PADPs to investigate the reciprocity between UL and DL channels from the perspective of the spatial distribution of MPCs, i.e., the multipath angles of arrival and departure. As shown in Fig. 15, the PADPs of both the UL and DL channels are displayed, measured in case 2 with the UE horn antenna rotated, and some dominant MPCs are indicated.

In TDD systems, the spatial characteristics of the UL and DL are nearly identical. In other words, the AAoA in the UL and AAoD in the DL are identical for the MPCs. However, in FDD systems, the spatial domains of the UL and DL are only partially identical. Similar multipath angles are observed at the LoS path (labeled as 1) and the forward and backward low-order reflective MPCs (labeled as 2, 3, 4, 5, 6, and 7). All of these are considered public MPCs with the same angle, although their power differs considerably. At the same time, there are also private MPCs that are observable only in specific frequency bands and angles. For instance, MPCs labeled as

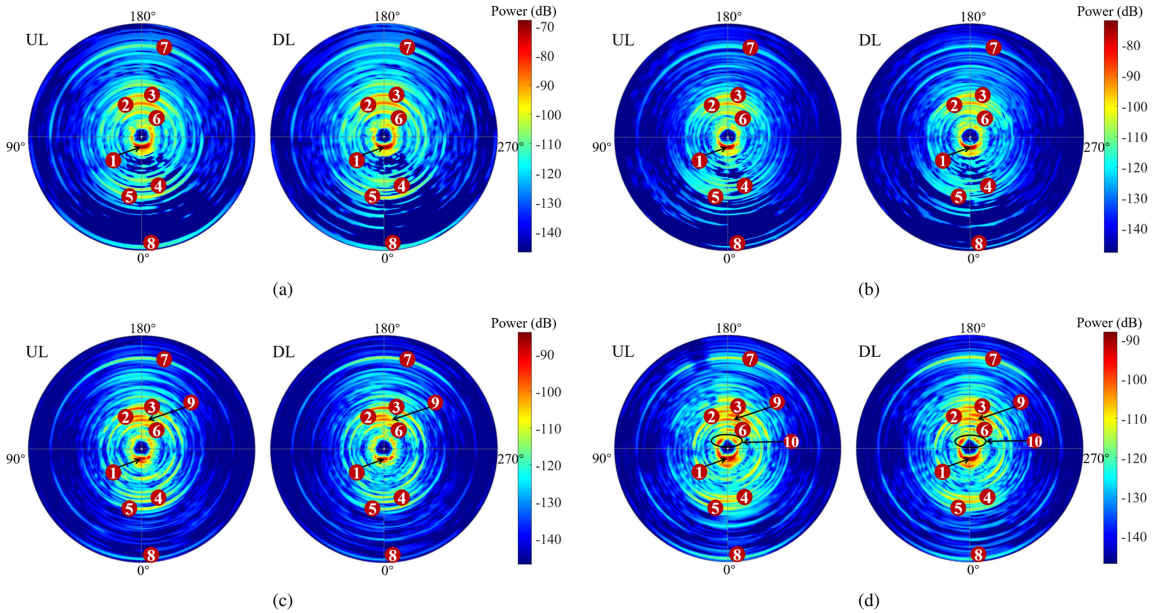

FIGURE 15. Measured multi-frequency PADPs of the UL and DL at the 5th measurement point in the LoS scenario. The angle on the circle indicates AAoD or AAoA, with 0° denoting the orientation where the UE horn antenna is directly aligned with the BS. The radial distance represents the delay of MPCs, while varying shades of color indicate the magnitude of received multipath power. Additionally, some dominant MPCs are labeled. (a) At 6 GHz. (b) At 6.5 GHz. (c) At 7 GHz. (d) At 7.5 GHz.

8 diminish in strength at 6.5 GHz, and MPCs labeled as 9 exist at 7 and 7.5 GHz but are absent at 6 and 6.5 GHz. The phenomenon is primarily attributed to two factors: Firstly, it is theorized that with increasing frequency, electromagnetic wave experiences greater attenuation, resulting in the attenuation of path power or disappearance of MPCs. Secondly, the constructive interference of MPCs in certain frequency bands leads to the emergence of newly visible MPCs at higher frequency bands, while the destructive interference of these MPCs at lower frequency bands results in the invisibility of MPCs.

Additionally, at 7.5 GHz, a distinctive path (labeled as 10) originating from the backward direction is identified, with angles spanning from 100° to 140° and 220° to 260°, and a delay falling between that of the LoS path and the first-order reflection path from the rear floor-to-ceiling window. This path is attributed to the diffuse scattering of the side wall, as only diffuse scattering can generate backward MPCs at such angles and delays in this particular scenario. This finding aligns with the conclusions drawn in the preceding APDP analysis.

In summary, in FDD systems, there are numerous public MPCs in the UL and DL channels with the same propagation delay and angle. These mainly include direct and low-order reflection MPCs, which constitute the majority of the channel power. Additionally, the different frequency bands of the UL and DL introduce several private MPCs that are exclusive to either the UL or DL, largely composed of diffuse and higher-order reflection MPCs. These public and private MPCs affect channel reciprocity by the magnitude of multipath power and their presence or absence, respectively.

VI. CONCLUSION

This article delves into the investigation of channel reciprocity within the 6 GHz band of TDD/FDD systems in indoor scenarios. Firstly, precise and impartial channel measurements were conducted for both the UL and DL channels in the 6 GHz band of TDD/FDD systems. Based on the measured data, an STDN algorithm is proposed to extract MPCs, establishing foundational support for a more equitable assessment of channel reciprocity. Then, a comprehensive analysis of the reciprocity between the UL and DL channels in TDD/FDD systems is conducted from four perspectives: path loss, delay spread, correlation coefficient, and multipath power differences. It can be concluded that TDD systems are nearly perfectly reciprocal, whereas FDD systems exhibit partial reciprocity in indoor scenarios. Specifically, near-identical path loss and delay spread are observed in TDD systems. In FDD systems, significant disparities are observed, with a maximum path loss difference of 16.66 dB in the UL and DL when the central frequency bands differ by 1.5 GHz. In terms of correlation coefficients, CBCCs in TDD systems exceed 95%, whereas in FDD systems, CBCCs range from 80% to 90%. Additionally, to depict the multipath power differences, a model illustrating MPD dependence on center frequency and frequency interval is established. The MPD dependency factors in LoS and NLoS scenarios are determined to be 5.81 and 4.59, respectively. Finally, factors influencing the reciprocity of FDD systems are analyzed from two perspectives: multipath delay and angle. Comparative analysis is conducted between measurement results and ray-tracing simulations, revealing the presence of numerous public MPCs in both the UL and DL. These MPCs share identical propagation delays and spatial

angles, constituting the majority of channel power. Additionally, a few private MPCs are observed, exclusively present in either the UL or DL. This study provides a solid foundation for channel estimation in FDD systems, namely, the reconstruction of the DL channel from the UL channel.

REFERENCES

[1] H. Miao et al., "Sub-6 GHz to mmWave for 5G-advanced and beyond: Channel measurements, characteristics and impact on system performance," *IEEE J. Sel. Areas Commun.*, vol. 41, no. 6, pp. 1945–1960, Jun. 2023.

[2] N. Li, C. Guo, and D. Wang, "Considerations on 6 GHz spectrum for 5G-advanced and 6G," *IEEE Commun. Standards Mag.*, vol. 5, no. 3, pp. 5–7, Sep. 2021.

[3] M. J. Marcus, "ITU WRC-19 spectrum policy results," *IEEE Wireless. Commun.*, vol. 26, no. 6, pp. 4–5, Dec. 2019.

[4] A. F. M. Shahen Shah, "A survey from 1G to 5G including the advent of 6G: Architectures, multiple access techniques, and emerging technologies," in *Proc. IEEE 12th Annu. Comput. Commun. Workshop Conf.*, 2022, pp. 1117–1123.

[5] Z. Zhang et al., "Adversarial training-aided time-varying channel prediction for TDD/FDD systems," *China Commun.*, vol. 20, no. 6, pp. 100–115, Jun. 2023.

[6] Z. Zhang, J. Zhang, Y. Zhang, L. Yu, and G. Liu, "AI-based time-, frequency-, and space-domain channel extrapolation for 6G: Opportunities and challenges," *IEEE Veh. Technol. Mag.*, vol. 18, no. 1, pp. 29–39, Mar. 2023.

[7] Y. Han, T.-H. Hsu, C.-K. Wen, K.-K. Wong, and S. Jin, "Efficient downlink channel reconstruction for FDD multi-antenna systems," *IEEE Trans. Wireless Commun.*, vol. 18, no. 6, pp. 3161–3176, Jun. 2019.

[8] Z. Liu et al., "Impact and compensation of I/Q imbalance on channel reciprocity of time-division-duplexing multiple-input multiple-output systems," *IET Commun.*, vol. 7, no. 7, pp. 663–672, May 2013.

[9] X. Jiang, M. Čirkić, F. Kaltenberger, E. G. Larsson, L. Deneire, and R. Knopp, "MIMO-TDD reciprocity under hardware imbalances: Experimental results," in *Proc. IEEE Int. Conf. Commun.*, 2015, pp. 4949–4953.

[10] W. Chen et al., "5G-advanced toward 6G: Past, present, and future," *IEEE J. Sel. Areas Commun.*, vol. 41, no. 6, pp. 1592–1619, Jun. 2023.

[11] Z. Zhang et al., "Deep reinforcement learning based dynamic beam selection in dual-band communication systems," *IEEE Trans. Wireless Commun.*, 2023, early access, Aug. 07, 2023, doi: 10.1109/TWC.2023.3300830.

[12] J. Dai, A. Liu, and V. K. N. Lau, "FDD massive MIMO channel estimation with arbitrary 2D-array geometry," *IEEE Trans. Signal Process.*, vol. 66, no. 10, pp. 2584–2599, May 2018.

[13] L. Bigler, H. P. Lin, S. S. Jeng, and G. Xu, "Experimental direction of arrival and spatial signature measurements at 900 MHz for smart antenna systems," in *Proc. IEEE 45th Veh. Technol. Conf.*, 1995, pp. 55–58.

[14] M. Alatossava, L. Hentila, V.-M. Holappa, and J. Meinila, "Comparison of outdoor to indoor and indoor to outdoor MIMO propagation characteristics at 5.25 GHz," in *Proc. IEEE 65th Veh. Technol. Conf.*, 2007, pp. 445–449.

[15] Y. Wang and Z. Shi, "Channel reciprocity and capacity analysis with outdoor MIMO measurements," in *Proc. IEEE 18th Int. Workshop Signal Process. Adv. Wireless Commun.*, 2017, pp. 1–5.

[16] K. Hugl et al., "Spatial reciprocity of uplink and downlink radio channels in FDD systems," in *Proc. COST*, 2002, Art. no. 066.

[17] D. Vasisht et al., "Eliminating channel feedback in next-generation cellular networks," in *Proc. Assoc. Comput. Machinery Special Int. Group. Data Commun. Conf.*, 2016, pp. 398–411.

[18] Z. Zhong, L. Fan, and S. Ge, "FDD massive MIMO uplink and downlink channel reciprocity properties: Full or partial reciprocity?," in *Proc. IEEE Glob. Commun. Conf.*, 2020, pp. 1–5.

[19] R. Schulpen et al., "Ambiguity in RMS delay spread of millimeter-wave channel measurements," in *Proc. 17th Eur. Conf. Antennas Propagat.*, 2023, pp. 1–5.

[20] S. Imtiaz, G. S. Dahman, F. Rusek, and F. Tufvesson, "On the directional reciprocity of uplink and downlink channels in frequency division duplex systems," in *Proc. IEEE 25th Int. Symp. Pers. Indoor Mobile Radio Commun.*, 2014, pp. 172–176.

[21] J. Zhang et al., "6–100 GHz research progress and challenges from a channel perspective for fifth generation (5G) and future wireless communication," *Sci. China Inf. Sci*, vol. 60, pp. 1–18, Jun. 2017.

[22] J. Zhang, Y. Zhang, Y. Yu, R. Xu, Q. Zheng, and P. Zhang, "3-D MIMO: How much does it meet our expectations observed from channel measurements?," *IEEE J. Sel. Areas Commun.*, vol. 35, no. 8, pp. 1887–1903, Aug. 2017.

[23] W. Ciccognani, A. Durantini, and D. Cassioli, "Time domain propagation measurements of the UWB indoor channel using PN-sequence in the FCC-compliant band 3.6-6 GHz," *IEEE Trans. Antennas Propag.*, vol. 53, no. 4, pp. 1542–1549, Apr. 2005.

[24] P. Tang, J. Zhang, A. F. Molisch, P. J. Smith, M. Shafi, and L. Tian, "Estimation of the K-factor for temporal fading from single-snapshot wideband measurements," *IEEE Trans. Veh. Technol.*, vol. 68, no. 1, pp. 49–63, Jan. 2019.

[25] S. Foo, M. A. Beach, P. Karlsson, P. Eneroth, B. Lindmark, and J. Johansson, "Spatio-temporal investigation of UTRA FDD channels," in *Proc. IEEE Int. Conf. 3G Mobile Commun. Technol.*, 2002, pp. 175–179.

[26] M. Steinbauer, A. F. Molisch, and E. Bonek, "The double-directional radio channel," *IEEE Antennas Propag. Mag.*, vol. 43, no. 4, pp. 51–63, Aug. 2001.

[27] P. Tang et al., "Channel measurement and path loss modeling from 220 GHz to 330 GHz for 6G wireless communications," *China Commun.*, vol. 18, no. 5, pp. 19–32, May 2021.

[28] R. Wang et al., "Enabling super-resolution parameter estimation for mm-wave channel sounding," *IEEE Trans. Wireless Commun.*, vol. 19, no. 5, pp. 3077–3090, May 2020.

[29] J. Zhang, C. Pan, F. Pei, G. Liu, and X. Cheng, "Three-dimensional fading channel models: A survey of elevation angle research," *IEEE Commun. Mag.*, vol. 52, no. 6, pp. 218–226, Jun. 2014.

[30] T. Jiang et al., "A study of uplink and downlink channel spatial characteristics in an urban micro scenario at 28 GHz," *Front. Inf. Technol. Electron. Eng.*, vol. 22, no. 4, pp. 488–502, Mar. 2021.

[31] H. Mi et al., "A novel denoising method based on machine learning in channel measurements," *IEEE Trans. Veh. Technol.*, vol. 71, no. 1, pp. 994–999, Jan. 2022.

[32] A. F. Molisch and M. Steinbauer, "Condensed parameters for characterizing wideband mobile radio channels," *Int. J. Wireless Inf. Netw.*, vol. 6, no. 3, pp. 133–154, Jul. 1999.

[33] ITU, "Multipath propagation and parameterization of its characteristics, REC. ITU-R P.1407-8," ITU, Geneva, Switzerland, Tech. Rep. P.1407-8, Sep. 2021.

[34] V. Cherkassky and Y. Ma, "Practical selection of SVM parameters and noise estimation for SVM regression," *Neural Netw.*, vol. 17, no. 1, pp. 113–126, 2004.

[35] E. B. Wilson and M. M. Hilferty, "The distribution of chi-square," *Proc. Nat. Acad. Sci.*, vol. 17, no. 12, pp. 684–688, Dec. 1931.

[36] R. Nitzberg, "Constant-false-alarm-rate signal processors for several types of interference," *IEEE Trans. Aerosp. Electron. Syst.*, vol. AES-8, no. 1, pp. 27–34, Jan. 1972.

[37] E. S. Sousa, V. M. Jovanovic, and C. Daigneault, "Delay spread measurements for the digital cellular channel in Toronto," *IEEE Trans. Veh. Technol.*, vol. 43, no. 4, pp. 837–847, Nov. 1994.

[38] 3rd Generation Partnership Project, "Study on channel model for frequencies from 0.5 to 100 GHz, version 16.1.0," 3GPP, Sophia Antipolis, France, Tech. Rep. 38.901, 2020. [Online]. Available: http://www.3gpp.org/DynaReport/38901.htm

[39] P. Kyosti et al., "WINNER II channel models," European Commission, Brussels, Belgium, Tech. Rep. IST-4-027756-WINNER, D1.1.2, Sep. 2007.

[40] Y. Wang et al., "Measurement-based analysis and modeling of channel characteristics in an industrial scenario at 28 GHz," in *Proc. IEEE 94th Veh. Technol. Conf.*, 2021, pp. 1–5.

[41] G. R. MacCartney, M. K. Samimi, and T. S. Rappaport, "Omnidirectional path loss models in new york city at 28 GHz and 73 GHz," in *Proc. IEEE 25th Int. Symp. Pers. Indoor Mobile Radio Commun.*, 2014, pp. 227–231.

[42] G. R. MacCartney, J. Zhang, S. Nie, and T. S. Rappaport, "Path loss models for 5G millimeter wave propagation channels in urban microcells," in *Proc. IEEE Glob. Commun. Conf.*, 2013, pp. 3948–3953.

[43] I. D. S. Batalha et al., "Large-scale modeling and analysis of uplink and downlink channels for LoRa technology in suburban environments," *IEEE Internet Things J.*, vol. 9, no. 23, pp. 24477–24491, Dec. 2022.
[44] Q. Song et al., "Modeling of path loss characteristics in a waveguide-like structure scenario at 28 GHz," in *Proc. IEEE 15th Eur. Conf. Antennas Propag.*, 2021, pp. 1–5.
[45] J. Zhang, H. Rohling, and Z. Ping, "Analysis of ICI cancellation scheme in OFDM systems with phase noise," *IEEE Trans. Broadcast.*, vol. 50, no. 2, pp. 97–106, Jun. 2004.
[46] J. Zhang, "The interdisciplinary research of Big Data and wireless channel: A cluster-nuclei based channel model," *China Commun.*, vol. 13, no. 2, pp. 14–26, Feb. 2016.
[47] A. Saleh and R. Valenzuela, "A statistical model for indoor multipath propagation," *IEEE J. Sel. Areas Commun.*, vol. 5, no. 2, pp. 128–137, Feb. 1987.
[48] A. Meijerink and A. F. Molisch, "On the physical interpretation of the Saleh–Valenzuela model and the definition of its power delay profiles," *IEEE Trans. Antennas Propag.*, vol. 62, no. 9, pp. 4780–4793, Sep. 2014.
[49] T. Jiang, J. Zhang, M. Shafi, L. Tian, and P. Tang, "The comparative study of S-V model between 3.5 and 28 GHz in indoor and outdoor scenarios," *IEEE Trans. Veh. Technol.*, vol. 69, no. 3, pp. 2351–2364, Mar. 2020.
[50] J. Zhang et al., "Deterministic ray tracing: A promising approach to THz channel modeling in 6G deployment scenarios," *IEEE Commun Mag.*, 2023.
[51] Remcom, "Wireless insite," Accessed on: Feb. 9, 2022. [Online]. Available: https://www.remcom.com/wireless-insite
[52] J. Zhang et al., "Channel measurement, modeling, and simulation for 6G: A survey and tutorial," May 2023, *arXiv:2305.16616.*
[53] D. Guven et al., "Methodology for measuring the frequency dependence of multipath channels across the millimeter-wave spectrum," *IEEE Open J. Antennas Propag.*, vol. 3, pp. 461–474, 2022.

HUIXIN XU (Graduate Student Member, IEEE) received the B.S. degree in communication engineering from Chongqing University of Posts and Telecommunications, Chongqing, China, in 2021. He is currently working toward the Ph.D. degree with the School of Information and Communication Engineering, Beijing University of Posts and Telecommunications, Beijing, China. His research interests include terahertz and massive MIMO channel measurements and modeling.

JIANHUA ZHANG (Senior Member, IEEE) received the Ph.D. degree in circuit and system from the Beijing University of Posts and Telecommunication (BUPT), Beijing, China, in 2003. She is currently a Professor with BUPT and the Director of the BUPT-CMCC Joint Research Center. She has published more than 200 articles and authorized 50 patents. She was the recipient of several paper awards, including the 2019 SCIENCE China Information Hot Paper, the 2016 China Comms Best Paper, and the 2008 JCN Best Paper. She was also recipient of several prizes for her contribution to ITU-R 4G channel model (ITU-R M.2135), the 3GPP Relay channel model (3GPP 36.814), and the 3GPP 3D channel model (3GPP 36.873). She was a Member of 3GPP 5G channel model for bands up to 100 GHz. From 2016 to 2017, she was the Drafting Group (DG) Chairperson of the ITU-R IMT-2020 (5G) channel model and led the drafting of IMT.2412 Channel Model Section. She is the Chairwomen of China IMT-2030 (6G) Tech Group–Channel Measurement And Modeling Subgroup and IEEE ComSoc Channel Modeling Subgroup. Her research interests include beyond 5G and 6G, artificial intelligence, data mining, especially in massive MIMO and terahertz channel modeling, channel emulator, and over-the-air (OTA) test. Dr. Zhang is a Fellow of the China Institute of Communications

PAN TANG (Member, IEEE) received the B.S. degree in electrical information engineering from the South China University of Technology, Guangzhou, China, in 2013 and the Ph.D. degree in Information and Communication Engineering from the Beijing University of Posts and Telecommunications (BUPT), Beijing, China, in 2019. From 2017 to 2018, he was a Visiting Scholar with the University of Southern California, Los Angeles, CA, USA. From 2019 to 2021, he was a Postdoctoral Research Associate with BUPT. He is an Associate Professor with the State Key Laboratory of Networking and Switching Technology, BUPT. He has authored and co-authored more than 40 papers in refereed journals and conference proceedings. His research interests include millimeter wave, terahertz, and visible light channel measurements and modeling.

LEI TIAN (Member, IEEE) received the B.S. degree in communication engineering and Ph.D. degree in information and communication systems from the Beijing University of Posts and Telecommunications (BUPT), Beijing, China, in 2009 and 2015, respectively. He is currently an Associate Professor with BUPT. His research interests include wireless channel measurement, modeling, and simulation for B5G and 6G, including millimeter wave, terahertz, massive MIMO, and satellite-to-ground.

QIXING WANG received the B.S., M.S., and Ph.D. degrees in information and communication engineering from the Beijing University of Posts and Telecommunications, Beijing, China, in 2002, 2005, and 2008, respectively. He is currently a Principal Member of Technical Staff responsible for 6G with the Future Research Laboratory, China Mobile Research Institute, Beijing. His research interests include virtual multi-input multi-output, holographic multi-input multi-output, and 4D-multi-input multi-output.

GUANGYI LIU (Member, IEEE) received the Ph.D. degree from the Beijing University of Posts and Telecommunications, Beijing, China, in 2006. He is currently a Chief Scientist with 6G, China Mobile Communication Corporation, the Co-chair of the 6G Alliance of Network AI (6GANA), the Vice Chair of THz Industry Alliance in China, and the Vice Chair of the Wireless Technology Working Group of IMT-2030 (6G) Promotion Group supported by the Ministry of Information and Industry Technology of China. He has been leading the 6G Research and Development of CMCC since 2018. He has acted as the Spectrum Working Group Chair and the Project Coordinator of LTE Evolution and 5G eMBB in Global TD-LTE Initiative (GTI) (2013–2020) and led the industrialization and globalization of TD-LTE evolution and 5G eMBB.